

Impact of Ionic Liquid Functionalized ZrO₂ Nanoparticles on Poly (stearyl methacrylate) Grafted Poly (vinylidene fluoride-co-hexafluoropropylene) Based Highly Conductive Gel Polymer Electrolytes for Lithium-Metal Batteries

Rittik Parui,^[a] Debalina Deb,^[b] Pallab Bose,^[a] and Subhratanu Bhattacharya*^[a]

In this study, an organic-inorganic hybrid polymer membrane is successfully designed and developed by grafting stearyl methacrylate (SMA) side chains onto the backbone of the P(VDF-HFP) copolymer followed by blending with varying amounts of imidazolium ionic liquids functionalized ZrO₂ nanoparticles. Different microporous gel polymer electrolytes (MGPEs) are prepared by immersing the membranes into a LiTFSI salt-dissolved ionic liquid electrolyte. The membranes' crystallinity, surface morphology, porosity, and thermal stability are investigated using various characterization techniques. The copolymer membrane blended with 60 wt% functionalized nanoparticles exhibits the highest porosity of 64.5%, which allows it to achieve a maximum electrolyte uptake of 387 wt%. That

enables the corresponding MGPE to achieve the highest room temperature lithium ion conductivity of $\sim 5.34 \times 10^{-3} \text{ S cm}^{-1}$ with a wide electrochemical stability window and good electrochemical stability against Li metal. Leveraging these advantageous characteristics, the lab-scale truly solid-state Li|MGPE|LiFePO₄ and Li|MGPE|LiNi_{0.8}Mn_{0.1}Co_{0.1}O₂ cells demonstrate excellent rate capability and reversible cycling stability while maintaining high specific capacities (up to 154 and 172 mAh g⁻¹, respectively, at 0.5 C) with >99.0% coulombic efficiency over 100 cycles. Such exceptional interfacial compatibility with both low- and high-voltage cathodes establishes the applicability of these newly developed MGPEs in next-generation all-solid-state lithium-metal batteries.

Introduction

Secondary lithium-ion batteries (LIBs) have received a lot of research attention due to their enticing properties in applications for large-scale energy storage, portable devices, and electric cars.^[1] Optimizing the active components in secondary batteries is the most popular way to increase their performance. Typically, a secondary battery consists of electrodes (the anode and cathode), an electrolyte, and a microporous separator membrane that serves the purpose of separating the anode and cathode to avoid the occurrence of a short circuit and to enable the transportation of charge carriers to achieve a complete circuit.^[2] The membrane's characteristics typically determine the final performance of a secondary battery. Therefore, the separator membranes used in secondary batteries should have strong electric insulation and good ion conductivity to achieve long cycle life, low self-discharging, high energy storage capability, high energy density, and safety.^[1b,2-3] The critical parameters that influence the efficiency of a separator are permeability, microstructure and porosity, electrolyte absorption and retention ability, and thermal and mechanical

stability.^[4] The level of porosity affects the ionic conductivity and electrochemical stability, which in turn are affected by the swelling process and the electrolyte uptake and retention ability of the separator.^[2]

In this regard the microporous gel polymer electrolytes (MGPEs), first introduced by Tarascon et al.,^[5] have produced promising results as both separators and electrolytes in secondary lithium batteries. In MGPEs, the liquid electrolyte is absorbed and held in the polymer membrane's pores (0.5–10 μm) by gelation. Because of the gelation effect, a larger amount of liquid electrolyte can be trapped in the polymer membrane without significantly impeding the mechanical stability, resulting in superior ion transport within the membrane.^[6]

Usually, MGPEs are activated by conventional commercial electrolytes containing lithium hexafluorophosphate (LiPF₆) salt in an aprotic solvent (ethylene carbonate (EC), propylene carbonate (PC), dimethyl carbonate (DMC), diethyl carbonate (DEC), etc.) or their mixture. These organic solvents decompose into volatile compounds at temperatures barely above the operating range for typical lithium-ion batteries.^[7] That often leads to internal short-circuiting and battery explosions.^[7-8] Room temperature ionic liquids (RTILs) are extensively studied as safer alternative electrolyte solvents for LIBs. RTILs have the ability to enhance the amorphous regions in polymer membranes by delaying the crystallization of polymer chains.^[9] They can also prevent the formation of dendrites on high-capacity lithium metal anodes, increasing the energy density and expanding the application range of the corresponding LIBs.^[10] However, IL electrolytes suffer from poor wetting with commer-

[a] R. Parui, Dr. P. Bose, Prof. S. Bhattacharya

Department of Physics, University of Kalyani, 741235 Kalyani, Nadia, West Bengal, India

E-mail: subhratanu1@gmail.com

[b] Dr. D. Deb

The Solid State and Structural Chemistry Unit (SSCU), Indian Institute of Science, 560012 Bangalore, India

 Supporting information for this article is available on the WWW under <https://doi.org/10.1002/batt.202300510>

cial separators, hindering the formation of MGPEs. Studies on cell components using IL electrolytes have revealed that the wetting issues in IL-electrolyte-based LIBs are most likely due to not getting compatible well with the separator rather than the electrodes.^[4b,11] Thus, a suitable IL-compatible separator membrane must be designed before employing IL-electrolytes in MGPEs.

As an MGPE host, semicrystalline fluoropolymers such as PVDF or its copolymer P(VDF-HFP) based membranes are considered one of the most potential candidates due to their brilliant film-forming ability, nonflammability, and excellent electrochemical stability.^[6b,12] However, the P(VDF-HFP) membrane alone usually suffers from several adverse properties, such as low porosity, high crystallinity, low mechanical strength, inherent inertness, low affinity for electrolyte solvents, etc.^[12b] Therefore, a variety of strategies, such as the phase inversion method,^[13] adding pore-forming agents,^[12b,14] blending with other polymers,^[15] crosslinking,^[14,16] using nanoparticles as fillers,^[17] and so on, have been implemented to improve the effectiveness of those fluoropolymer based membranes as the host for MGPE. However, disadvantages associated with some of the MGPEs obtained from the membranes, including particle aggregation, poor electrolyte uptake and retention, low electrochemical stability, and low lithium-ion conductivity, make them impractical for application in LMBs. Consequently, there is a growing interest in creating MGPEs devoid of these shortcomings.

One of the most effective approaches in this field has been the development of organic-inorganic hybrid microporous polymer membranes, owing to their improved porosity, low crystallinity, and optimum thermal and mechanical stability.^[12b,18] In this regard, employing functionalized fluoropolymers, made by grafting functional groups or polymeric side chains to the backbones of the host polymer becomes a more effective strategy.^[18a] On the other hand, the ionic liquid functionalized nanoparticles, formerly referred to as nanoscale hybrid ionic liquid (NHIF),^[19] can be effectively used as the pore-forming agent, similar to the earlier report on P(VDF-HFP)-based MGPE.^[12b] The hybrid polymer membranes are unique from others owing to their advantage of design flexibility, which is achieved by adjusting the organic and inorganic fractions based on demand. In addition, the free radical polymerization process makes adjusting the degree of functionalization simple. Together, the distinctive qualities of the organic and inorganic components result in grafted hybrid membranes exhibiting superior mechanical, thermal, dielectric, and hydrophobic properties and a better solvent absorption capability than pure polymers. The ease with which microporous membranes can be converted into gel polymer electrolytes by soaking the membrane in liquid electrolytes without sacrificing their mechanical stability is another noteworthy feature. The resultant MGPEs may successfully hold the electrolyte solutions inside the polymeric network architecture's pores without leaking, preventing the risk of a short circuit, fire, or explosion during a battery malfunction.

Inspired by the above concepts, we have developed a new class of efficient, crosslinked nanocomposite copolymer mem-

brane-based MGPEs for high-performance lithium-ion batteries. The primary copolymer membrane is prepared by grafting stearyl methacrylate (SMA) side chains to the P(VDF-HFP) copolymer backbone using free radical polymerization. It was previously observed that the bulky non-polar units (C_{18}) of SMA effectively suppress the propensity for crystallization of the semicrystalline polymer and also improve mechanical stability.^[20] IL-functionalized zirconium oxide (ZrO_2) nanoparticles ($ZrO_2\text{-NHIF}$) are used as inorganic pore-forming agents to modify the copolymer membrane. The microporous nanocomposite copolymer membranes display low crystallinity, broad thermal stability, excellent mechanical properties, high solvent uptake, and retentivity. The nanocomposite membranes are swollen in 0.5 M LiTFSI salt-dissolved imidazolium-based IL electrolyte to prepare MGPEs. The MGPEs formed by 60 wt% NHIF incorporated membrane display the highest ionic conductivity (~5.34 mS/cm) at room temperature (303 K), a wide electrochemical stability window (>5.1 V), and high Li^+ ion transfer ability ($t_{Li}^+ \approx 0.64$) with wonderful electrochemical stability against Li-metal. Impressive rate performance allied with the high Coulombic efficiency of Li/MGPE/LiFePO₄ batteries and high voltage Li/MGPE/LiNi_{0.8}Mn_{0.1}Co_{0.1}O₂ batteries confirm the application potentiality of the MGPEs in all-solid-state lithium batteries.

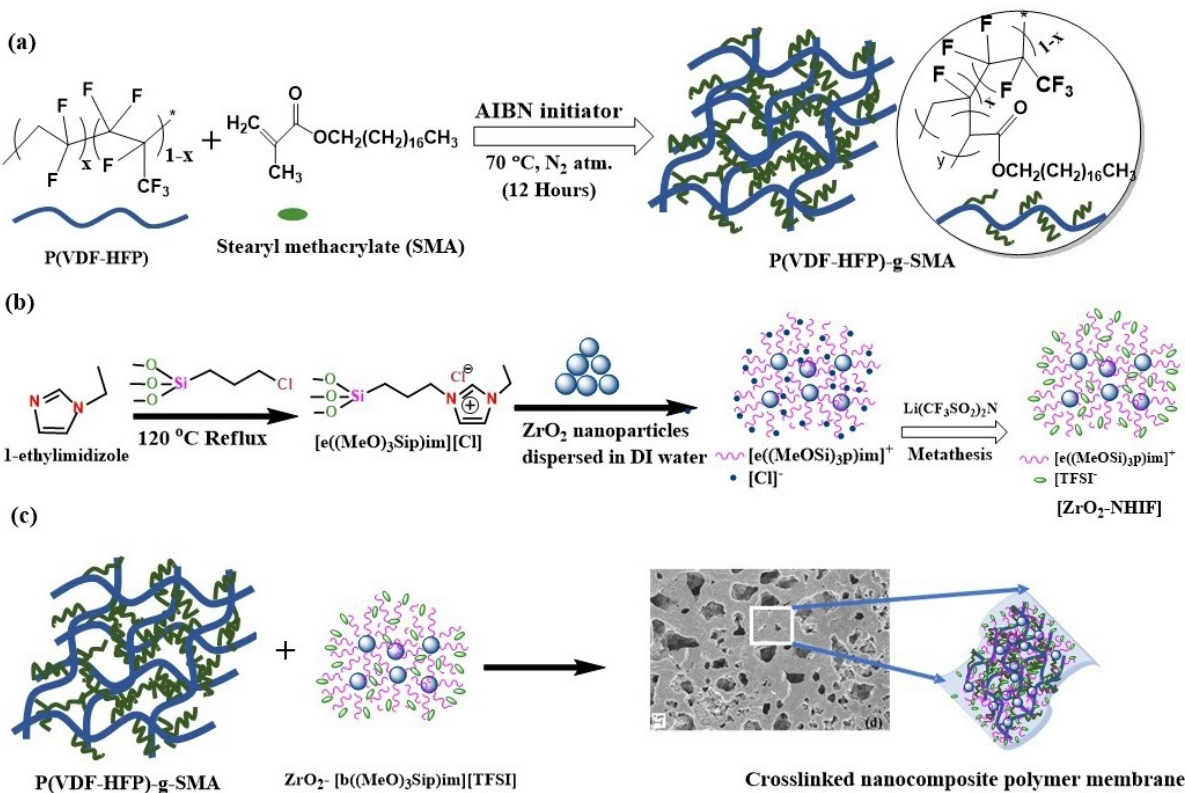
Experimental Section

Materials

P(Vdf-HFP) (average mol. wt. 455,000 g mol⁻¹), Zirconium (IV) butoxide, 2, 2-azobisisobutyronitrile (AIBN), N-methyl-2-pyrrolidone (NMP) (anhydrous, 99.5%), and acetone (analytical grade, H₂O < 0.02%) were purchased from Sigma-Aldrich and used without further purification. Lithium bis (trifluoromethane sulfonamide) (LiTFSI) (99.95%) was purchased from Sigma-Aldrich and dried at 120°C under vacuum for 12 h before use. Stearyl Methacrylate (SMA) (mol. wt. 338 g mol⁻¹), 1-ethylimidazole (>98%), and (3-Chloropropyl) trimethoxysilane (>97%), 1-ethyl-3-methylimidazolium bis(trifluoromethane sulfonamide) ([EMIM][TFSI]) (>98.0%) was procured from TCI Chemicals. All other reagents and solvents were obtained from local commercial sources and used as received. Before use, P(Vdf-HFP) and [EMIM][TFSI] were vacuum dried at ~10⁻³ torr for 48 h to remove moisture and were stored in an Argon gas-filled glove box (Vigor Tech, H₂O < 0.5 ppm, O₂ < 0.5 ppm).

Synthesis of P(Vdf-HFP)-g-PSMA copolymer

The P(Vdf-HFP)-g-PSMA copolymer was synthesized via the free radical polymerization method using AIBN as the initiator, as shown in Scheme 1(a). In a typical reaction, 2.55 g (85 wt.%) P(Vdf-HFP) and 0.525 mL (15 wt.%) stearyl methacrylate were dissolved in 30 mL of ethyl acetate in a round-bottom flask under vigorous stirring at 50°C to form a homogenous solution. Subsequently, 0.5 wt% AIBN was added to the solution. The flask was sealed with a rubber plug, and the oxygen inside the flask was carefully evacuated by the back-filling process using N₂ gas three times. The mixture was heated at 70°C under constant stirring to carry out the polymerization reaction. After 12 hours, the products were dissolved in tetrahydrofuran (THF) and precipitated in petroleum



Scheme 1. A) Grafting of SMA chains on the P(VDF-HFP) copolymer backbone, B) Preparation of ZrO₂-NHIF, C) Preparation of crosslinked nanocomposite copolymer membranes.

ether. The process was repeated three times to obtain a pure P(Vdf-HFP)-g-PSMA graft copolymer. Finally, the resulting copolymer was dried at 85 °C under vacuum for 12 hours and kept in a dry box for further use. Similar grafting of side chains on the polymer backbone using the free radical polymerization method was also adopted by other researchers.^[14,20–21]

Synthesis of ZrO₂ nanoparticles and ZrO₂-NHIF

ZrO₂ nanoparticles were prepared according to the procedure described in the supporting information, as reported earlier.^[22] The preparation of ionic liquid functionalized ZrO₂ nanoparticles, a class of nanoscale hybrid ionic fluid (NHIF), was carried out according to our previously reported methods^[19a,b,23] as described schematically in Scheme 1b. Briefly, an equimolar amount of 1-ethylimidazole and (3-chloropropyl) trimethoxysilane were dissolved in dimethylformamide (DMF). The solution was refluxed at 110 °C for three days under an N₂ atmosphere. A viscous and yellowish IL (1-ethyl 3-propyl (trimethoxysilyl) imidazolium chloride ([EmImSi(OMe)₃][Cl]) was collected and purified via liquid extraction in diethyl ether. ¹H NMR (Figure S1) (400 MHz, DMSO d₆): δ (ppm)= 9.08 (1H, brs), 7.88 (1H, brs), 7.63 (1H, brs), 4.23 (2H, brs), 4.05 (2H, brs), 3.55 (9H, s), 1.71 (2H, brs), 1.44 (3H, brs), 0.52 (2H, brs).

For surface functionalization of ZrO₂ nanoparticles, an excess amount of [EmImSi(OMe)₃][Cl] IL was allowed to react with an aqueous dispersion of ZrO₂ nanoparticles under continuous stirring at 80 °C for 12 h. Finally, an aqueous solution of an excess amount of LiTFSI salt was added to the mixture under continuous stirring for anion exchange. The hydrophobic, [EmImSi(OMe)₃][TFSI] IL tethered ZrO₂ nanoparticles (ZrO₂-NHIF) were separated from the bottom of the container after 3 hours. The ZrO₂-NHIF was collected

after repeated washing with distilled water, dried under vacuum at 100 °C, and stored in the Argon-filled glove box for further use.

Preparation of nanocomposite copolymer membranes and MGPE

The nanocomposite copolymer membranes were prepared by blending the synthesized P(Vdf-HFP)-g-PSMA copolymer with different wt.% of ZrO₂-NHIF (Scheme 1c). In a typical process, the graft copolymer was dissolved in an appropriate amount of acetone under continuous stirring at a slightly elevated temperature. After complete dissociation of the copolymer, different wt.% of ZrO₂-NHIF (Table 1) were slowly added to the solution. After 8 hours of continuous stirring, the solvent was slowly evaporated, and the resulting slurries were coated as membranes of thickness ~50 μm on a cleaned glass plate using a micrometer adjustable film applicator. After vacuum drying at 70 °C overnight, the free-standing membranes were collected and kept in a dry box for further use.

The MGPEs were prepared by soaking the nanocomposite membranes in 0.5 M LiTFSI salt dissolved in [EmIm][TFSI] IL for 1 hour. Four MGPEs were developed in this method and are labeled as MGPEX, with X=0, 20, 40, and 60, respectively (Table 1). Pure P(VDF-HFP) copolymer membrane and corresponding GPE were also prepared following a similar procedure for comparison. All the above procedures for preparing the electrolytes were carried out in an argon-filled glove box.

Table 1. Different crosslinked nanocomposite membranes and corresponding MGPEs with the percentage of different components.

P(Vdf-HFP)-g-PSMA (wt.%)	ZrO ₂ -NHIF (wt.%)	Crosslinked Nanocomposite membrane	Soaked in	MGPE
100	0	P(VDF-HFP)-g-PSMA	0.5 M LiTFSI in [EMIM][TFSI] IL	MGPE0
80	20	PVSMA20NHIF		MGPE20
60	40	PVSMA40NHIF		MGPE40
40	60	PVSMA60NHIF		MGPE60

Characterizations

The successful synthesis and purity of the P(VDF-HFP)-g-PSMA graft copolymer and [EmImSi(OMe)₃][TFSI] IL were confirmed by ¹H NMR using a Bruker Avance-400 MHz NMR Spectrometer. The dispersion of ZrO₂ nanoparticles was analyzed using high-resolution transmission electron microscopy (HR-TEM) (JEOL JEM-2100, 200 kV). The structure of the copolymer membranes was characterized by an X-ray diffraction (XRD) study using a Rigaku Miniflex 600 diffractometer with Cu K α radiation ($\lambda=0.154$ nm) at a scan rate of 0.25°/min.

The morphology and porosity of the nanocomposite copolymer membranes were investigated by field-emission scanning electron microscopy (FE-SEM), Supra 55 (Germany), with Air Lock.

Fourier-transform infrared (FT-IR) spectroscopy of the samples was carried out using a Shimadzu IR affinity 1S FT-IR spectrometer fitted with a single-reflection diamond attenuated total reflection (ATR) sampling module to identify various interactions within the membranes. The spectra were acquired in the wave number range of 400 to 4000 cm⁻¹ by averaging 64 scans at a resolution of 4 cm⁻¹.

Thermogravimetric analysis (TGA) was performed on a Netzsch TG 209 F3 Tarsus system within a temperature range from room 30 to 600°C at a heating rate of 10°C/min in a dry N₂ environment. The differential scanning calorimetry (DSC) was performed using a differential scanning calorimeter (Netzsch DSC 214, Polyma) in a dry N₂ environment. The DSC scans were recorded for different phase transitions within the membrane at a constant heating/cooling rate of 10°C/min, in the temperature range of 60 to 200°C. Before measurement, both the temperature and enthalpy of the DSC were auto-calibrated by pure indium.

Electrical and electrochemical measurements

The temperature-dependent dc ionic conductivity (σ_{dc}) of different MGPEs was evaluated by analyzing the ac conductivity data obtained from the impedance spectroscopy measurement. The measurement was carried out using a Hioki LCR meter model IM3536 over the frequency range of 42 Hz to 8 MHz with an amplitude of 5 mV and in the temperature range from -20°C to 100°C. The copolymer membranes were first immersed in the electrolyte solution for 2 hours inside the glove box to become MGPEs and then assembled into a symmetrical stainless steel (SS) cell (SS/MGPE/SS). The temperature was controlled using a Eurotherm temperature controller with a temperature constancy of ±0.1°C. The measurement was carried out in a dynamic vacuum.

The electrochemical stability window (ESW) of the MGPEs was measured by a linear sweep voltammetry (LSV) test using an electrochemical analyzer (Bio-Logic, model SP-150). The MGPEs were sandwiched between SS (the working electrode) and lithium (which served as both counter and reference electrodes) (Li/MGPE/SS) at a scan rate of 5 mV s⁻¹ in the voltage range of -0.5–6.0 V.

The lithium-ion transference number (t_{Li}^{+}) of the MGPEs was evaluated at room temperature by a combined chronoamperometry and electrochemical impedance spectroscopy (EIS) technique, which was carried out using an electrochemical analyzer (Bio-Logic, model SP-150). In this experiment, a Li/MGPE/Li symmetrical cell was polarized by a DC voltage pulse of 10 mV, and the corresponding initial (I_0) and steady-state (I_s) polarization currents were recorded. The cell's initial (R^0) and steady-state (R^S) interfacial impedances were also measured. The transference number (t_{Li}^{+}) was estimated by Eq. (2), proposed by Evans and Bruce,^[24] as

$$t_{Li}^{+} = \frac{[I^S(\Delta V - I^0 R^0)]}{[I^0(\Delta V - I^S R^S)]} \quad (1)$$

Galvanostatic cycling tests on symmetric Li/MGPE/Li symmetric cells were carried out using the electrochemical workstation (Bio-Logic, model SP-150). The current density used for the Li-metal plating and stripping was 0.3 mA cm⁻² (corresponding to 1 h 'charge' and 1 h 'discharge') with cutoff voltages of +0.5 V and -0.5 V vs. Li⁺/Li.

The electrochemical performances of the electrolytes were investigated in lab-scale LiFePO₄/MGPE/Li and LiNi_{0.8}Mn_{0.1}Co_{0.1}O/MGPE/Li battery prototypes prepared in an argon-filled glove box. The LiFePO₄ (LFP) cathode was prepared by mixing battery grade LFP powder (MTI Corporation, USA), super P, and PVDF (binder) in a ratio of 8:1:1 in N-methyl-2-pyrrolidone (NMP) solvent and by hand milling to obtain a viscous slurry. The slurry was cast onto an aluminum current collector using a doctor's blade. NMP solvent was removed by evaporation at ambient temperature for 12 h and drying at 100°C for 12 h. The loading of the active material on the electrode was ca. 2.5–3.0 mg. The LiNi_{0.8}Mn_{0.1}Co_{0.1}O (NMC-811) cathode was prepared following the similar procedure described for the LFP cathode. Lab-scale LFP/MGPE/Li and NMC/MGPE/Li cells were galvanostatically cycled on a Biologic BCS-810 multi-potentiostat within a potential range of 2.5–4.2 V vs. Li⁺/Li at different C rates. EIS measurement was used to analyze the electrochemical kinetic properties of the cell. Cyclic voltammetry (CV) was performed for the Li/MGPE60/LFP cell at a scan rate of 0.1 mV s⁻¹ in the voltage range of 2.1–4.2 V vs Li⁺/Li.

Results and Discussion

Synthesis and characterization of P(VDF-HFP)-g-PSMA copolymer

The overall synthetic pathway of crosslinked copolymer and nanocomposite copolymer membranes is outlined in Scheme 1a-c. In the first step, stearyl methacrylate (SMA) chains were successfully grafted onto the P(VDF-HFP) copolymer backbone at a fixed monomer – to – copolymer ratio (15:85) (w/w) via free radical copolymerization (Scheme 1a). The as

prepared P(VDF-HFP)-g-PSMA membrane was blended with different weight percentages of $\text{ZrO}_2\text{-NHIF}$ (Scheme 1b and 1c) to obtain four different microporous crosslinked nanocomposite copolymer membranes. The MGPEs were prepared by soaking the nanocomposite copolymer membranes in 0.5 M LiTFSI in $[\text{EMIM}][\text{TFSI}]$ IL electrolyte. The classification of nanocomposite copolymer membranes and MGPEs is shown in Table 1.

The successful graft copolymerization of SMA has been confirmed using ^1H NMR and ATR-FT-IR spectroscopy. Figure 1a presents a comparison of ^1H -NMR spectra for P(VDF-HFP) and P(VDF-HFP)-g-PSMA. The peaks at $\delta=2.5$ and 3.5 ppm observed in both spectra appear to be due to the solvents DMSO D_6 and water, respectively. The ^1H NMR spectrum for P(VDF-HFP) exhibits a singlet at $\delta=2.26$ ppm and multiplets at $\delta=2.8\text{--}2.9$ ppm, which are attributable to the respective head-to-head or tail-to-tail (hh) stereo regularity and the head-to-tail (ht) bonding arrangement originated from the vinylidene fluoride (VDF) segment of the P(VDF-HFP) copolymer, respectively.^[25] The P(VDF-HFP)-g-PSMA graft copolymer spectrum exhibits additional signals corresponding to stearyl methacrylate.^[20,25b] The methyl group in $-(\text{CH}_2)_{15}\text{CH}_3$ of the stearyl shows responses at $\delta=0.88$. The chemical shifts observed within $\delta=1.31\text{--}1.43$ ppm occur due to protons in the long-chain methylene bands ($\text{CH}_2)_{15}\text{CH}_3$ of the stearyl. The protons of the methylene in

the backbone ($-\text{CH}_2(\text{CH}_2)_{15}\text{CH}_3$) and those of the methylene connected with the carbon atom of stearyl ($-\text{CH}_2\text{C}-$) showed chemical shifts within $\delta=1.78\text{--}1.58$ ppm. Finally, the H of the methylene group adjacent to the oxygen atom of stearyl ($-\text{OCH}_2-$) shows a chemical shift at ($\delta=4.13$ ppm).

Figure 1b demonstrates a comparison of FT-IR spectra for P(VDF-HFP) and P(VDF-HFP)-g-PSMA copolymers. The spectrum of the P(VDF-HFP) exhibits characteristic peaks corresponding to CH_2 wagging, antisymmetric CF_2 stretch, and CF_3 out-of-plane deformation at 1401, 1172, and 1061 cm^{-1} , respectively,^[25c] The bands located at 974 and 762 cm^{-1} and a small band at 854 cm^{-1} are assigned to the non-polar and most thermodynamically stable α -phase conformations of P(VDF-HFP).^[26] Conversely, the small peak near 840 cm^{-1} indicates the existence of polar (β -phase) conformation in the copolymer.^[25c,26] The band observed at $\sim 873 \text{ cm}^{-1}$ is attributed to the amorphous part of the copolymer.^[25c,26] The spectrum of P(VDF-HFP)-g-PSMA contains an additional band at 1730 cm^{-1} , corresponding to the stretching mode of carbonyl groups (C=O) associated with the poly stearyl methacrylate side chains.^[27] Thus, both ^1H NMR and FT-IR studies confirm that PSMA side chains were successfully grafted onto the backbone of the P(VDF-HFP) copolymer.

Structural and thermal properties analysis of membranes

The synthesized ZrO_2 nanoparticles were characterized using X-ray diffraction spectroscopy (Figure S2).

The morphologies of as-synthesized ZrO_2 nanoparticles and $\text{ZrO}_2\text{-NHIF}$ were analyzed using HR-TEM, as shown in Figures 2a and 2b, respectively. The ZrO_2 nanoparticles exhibit high monodispersity as well-distributed nanospheres with an average diameter of $\sim 20\text{--}22$ nm. The clear lattice fringes with a lattice spacing of ~ 0.317 nm correspond to the (-111) reflecting plane of monoclinic ZrO_2 nanocrystals. Observed limited aggregation of the nanospheres after surface functionalization confirms the viability of the chosen method to functionalize the nanoparticles. Figures 2c and 2d depict the low and high magnification images of the dispersion of ZrO_2 nanoparticles comprising the highest wt.% of $\text{ZrO}_2\text{-NHIF}$ (PVSMA60NHIF). As observed from the figures, small clusters of ZrO_2 nanoparticles with an overall dimension ranging from 100 to 300 nm are spread fairly uniformly throughout the membrane.

Figure 3a presents the XRD spectra of P(VDF-HFP), P(VDF-HFP)-g-PSMA, and different wt% of $\text{ZrO}_2\text{-NHIF}$ blended nanocomposite membranes. In order to quantitatively analyze the reflected peak positions, deconvolution of the spectra within the 2θ range from 15.6° to 22.5° is carried out, and the results are presented in Figure 3b. The deconvolution was performed by fitting the spectra to the superposition of Gaussian functions and determining the integrated peak areas. The diffraction pattern of pure P(VDF-HFP) displays typical semicrystalline behavior with overwhelming diffraction peaks at $2\theta=18.2^\circ$, 19.9° and 26.7° , conforming to the (100), (020), and (110) monoclinic crystal planes of non-polar α -PVDF.^[6b,28] After the grafting of PSMA side chains, these peaks become relatively

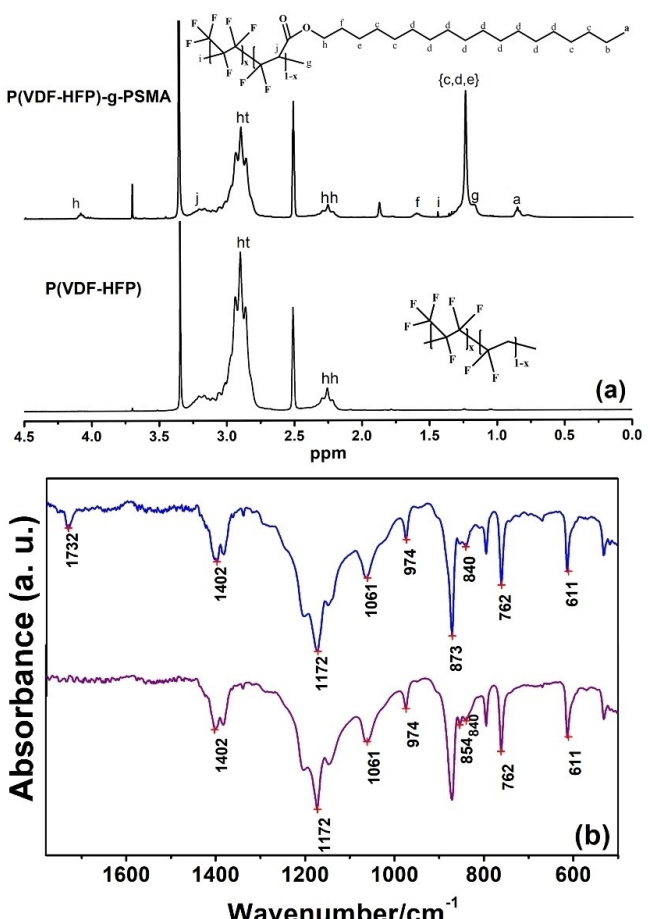


Figure 1. Comparison of A) ^1H -NMR and B) FT-IR spectra of SMA-grafted P(VDF-HFP) and pure P(VDF-HFP).

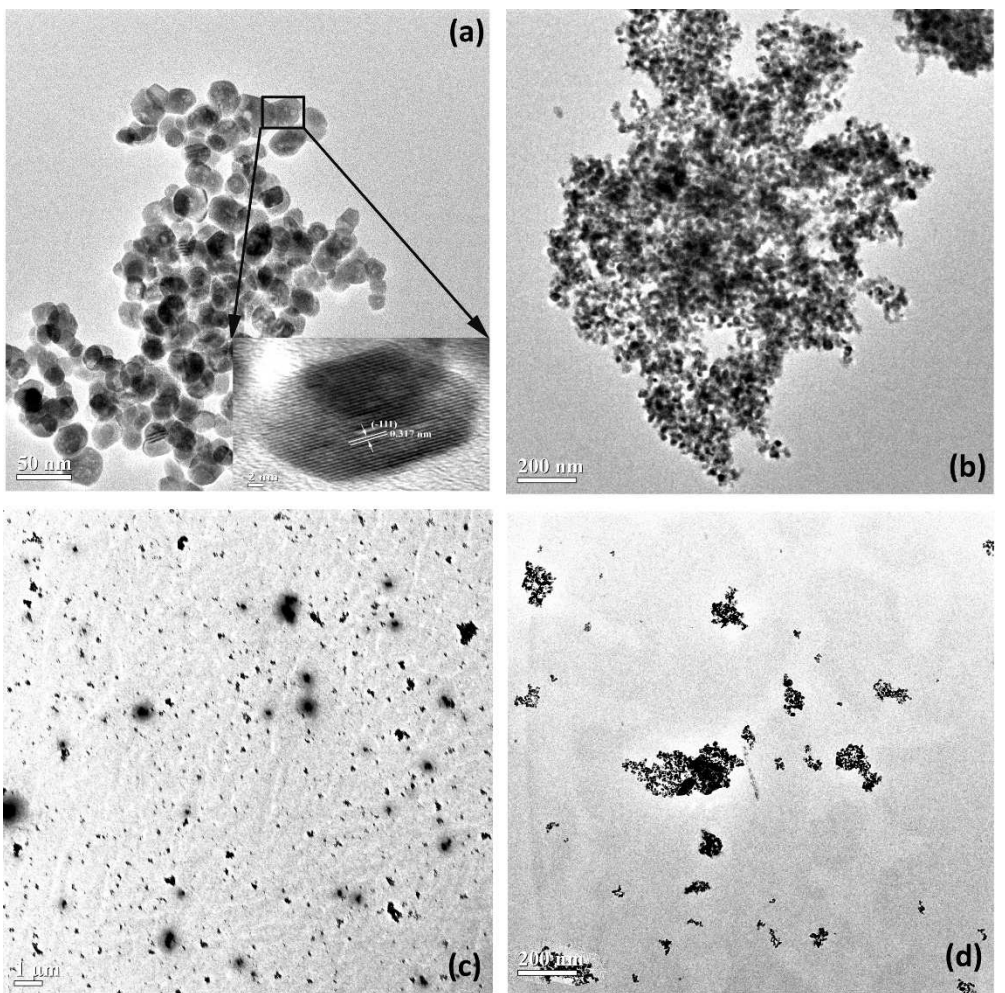


Figure 2. TEM bright-field images of A) as synthesized and B) surface functionalization of ZrO_2 nanoparticles and high-resolution image (inset).

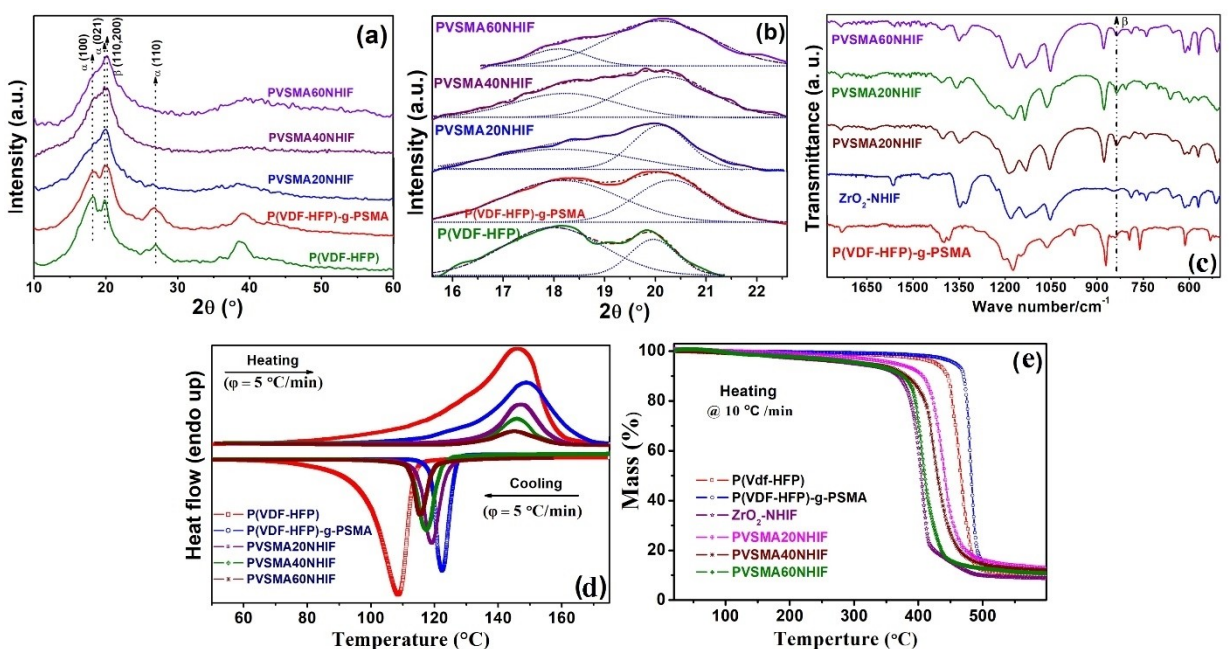


Figure 3. A) X-ray diffraction profile and B) deconvoluted region of the spectra within the 2θ region 15.6 to 22.5 for different copolymer membranes. C) FTIR transmission spectra; D) DSC heating and a cooling scan; and E) TGA profiles of different membranes.

weak. Moreover, the peak at $2\theta=19.9^\circ$ is broadened. These suggest that the grafting of SMA chains significantly affects the crystalline phase of P(VDF-HFP). The diffraction profiles of the nanocomposite membranes indicate a phase transformation of the crystalline structure. With the increase in NHIF content, the area under (100) reflection plane gradually reduce and a new peak at $2\theta=20.27^\circ$ corresponding to the sum of the reflection from (110) and (200) planes of the electroactive β -phase of PVDF^[28] evolves. All the observed features indicate that ZrO_2 -NHIF influences the re-crystallization kinetics of the VDF matrix and transforms the basic non-polar α -conformation of PVDF into an electroactive β -phase. It also improves the localized amorphous regions within the copolymer.

Figure 3c displays the FT-IR spectra of different nanocomposite membranes, including P(VDF-HFP)-g-PSMA, within the wavenumber range of 500 to 1780 cm⁻¹. The spectrum of ZrO_2 -NHIF is also included in the figure. As shown, the spectrum of ZrO_2 -NHIF comprises absorption bands between 600–618 cm⁻¹, which are attributable to the Zr–O–Si symmetric stretching vibration, Si–O stretching vibrations, and CH₂ and CH₃ scissoring vibrations, respectively.^[12b,29] The band observed at $\nu=654$ cm⁻¹ resembles the C–H vibrational mode of the cyclic methylimidazolium group.^[12b] The bands at $\nu=740$ and 789 cm⁻¹ are ascribed to the overlapping of the symmetric bending mode of –CF₃ and combined stretching mode vibrations of C–S and S–N bonds, respectively.^[29] Finally, the vibrational bands observed in the range 1050–1150 cm⁻¹ and at $\nu=1563$ cm⁻¹ are aroused due to the asymmetric stretching mode of TFSI⁻ anions and to the interaction between the C–C and C–N bending modes of vibrations, respectively.^[12b] In the spectra of nanocomposite membranes, the majority of the bands associated with ZrO_2 -NHIF and the bands corresponding to the various vibrational modes of P(VDF-HFP)-g-PSMA discussed earlier are present. However, the bands designating the α -phase of P(VDF-HFP), visible in the spectrum of P(VDF-HFP)-g-PSMA, were completely absent in the spectra. Moreover, the feeble band at 840 cm⁻¹ observed in the spectrum of the graft copolymer, ascribing to the electroactive β -phase of PVDF, progressively gets stronger with the increasing weight percentage of NHIF. The observed change in conformation may be attributed to the strong dipole-dipole interaction between the Si–O dipole of NHIF and the >CF₂ dipole of the P(VDF-HFP) backbone, as observed earlier for other NHIF-blend gel polymer electrolytes.^[12b]

DSC thermograms of P(VDF-HFP), P(VDF-HFP)-g-PSMA, and different NHIF blended nanocomposite membranes are de-

picted in Figure 3d. Various parameters related to phase transitions, as obtained from the analysis of DSC profiles for different samples, are listed in Table 2. Each of the DSC profiles shows a single melting and crystallization peak. The crystallization temperature of the crosslinked copolymer ($T_c=122$ °C) is significantly higher as compared to PVDF-HFP ($T_c=108$ °C). However, the enthalpy value, i.e., the area under the curve corresponding to either crystallization (ΔH_c) or the corresponding melting endotherm (ΔH_m) decreases. Thus, due to crosslinking, although the rate of crystallization transition increases, but it may produce incomplete crystals, which ultimately reduces the overall crystallinity of the copolymer. Increasing NHIF content gradually shifts T_c to a lower temperature with decreasing enthalpy. Thus, NHIF delays the crystallization transitions within the copolymer, which is analogous to the earlier reports.^[19a]

The absolute crystallinity fraction is estimated as^[30]

$$X_c = \frac{\Delta H_m}{\Delta H_m^0} \times 100\% \quad (2)$$

where ΔH_m^0 is the extrapolated enthalpy corresponding to the melting of 100% crystalline PVDF [104.7 J/g].^[31] The degree of crystallinity (X_c) decreases from ~25% for pure P(VDF-HFP) to ~5.8% for PVSMA60NHIF (Table 2). Thus, NHIF in the membranes not only delays the phase transition but also effectively reduces the crystallinity of the copolymer. Earlier studies have shown that the amorphous areas of polymer matrix are beneficial for ion conduction.^[32] Therefore, compared to other membranes, the PVSMA60NHIF membrane may offer better ion-conduction ability since it has the most amorphous region in its matrix.

The thermal stability of different samples was evaluated using a thermogravimetric analyzer (TGA). Figure 3e illustrates the TGA profiles of different copolymer membranes from room temperature to 600 °C. The TGA profile of ZrO_2 -NHIF is also included. The thermal decomposition of both P(VDF-HFP) and SMA-grafted copolymers is in a single step. However, after crosslinking, the decomposition temperature slightly elevated from ~440 °C to ~465 °C, indicating that the crosslinking has improved the thermal stability of the copolymer. As the thermal stability of the NHIF is lower (~380 °C) than that of the copolymer, with increasing NHIF blending, the thermal stability of the nanocomposite membranes slightly decreases. However, the membrane comprising the highest wt% of NHIF (PVSMA60NHIF) exhibits thermal stability up to ~396 °C, which

Table 2. Degree of crystallinity and DSC-related data of as-synthesized nanocomposite membranes.

Sample	T _m (°C)	T _c (°C)	ΔH _m (J/g)	ΔH _c (J/g)	Crystallinity (X _c %)	Pore size (from SEM) (μm)	Porosity (%) from solvent uptake
P(VDF-HFP)	145.8	108.2	26.2	25.9	25.0	3.46	8.7
P(VDF-HFP)-g-PSMA	148.6	122.5	21.73	20.9	20.7	6.65	20.9
PVSMA20NHIF	146.8	119.1	14.14	13.83	13.5	11.13	37.9
PVSMA40NHIF	145.5	117.1	10.63	10.5	10.1	14.37	53.4
PVSMA60NHIF	144.7	115.2	6.03	5.3	5.8	17.02	64.5

confirms that the nanocomposite membranes are suitable and safe for high-temperature applications.

Mechanical stability, Morphology, porosity, and solvent uptake

The nanocomposite copolymer membranes are visually observed to be free-standing, semi-transparent, flexible, and have

a smooth surface texture due to crosslinking. The mechanical flexibility of the membranes has been evaluated by stretching, bending, and twisting them, as shown in Figure 4a-d for PVSMA60NHIF. The membranes have been found to recover their original shapes after releasing external stress.

The porosity and pore structure of the polymer membrane substantially impact its ability to absorb and retain liquid electrolytes. The FE-SEM images (Figures 5a and b) indicate that the porous structure of P(VDF-HFP) was substantially modified

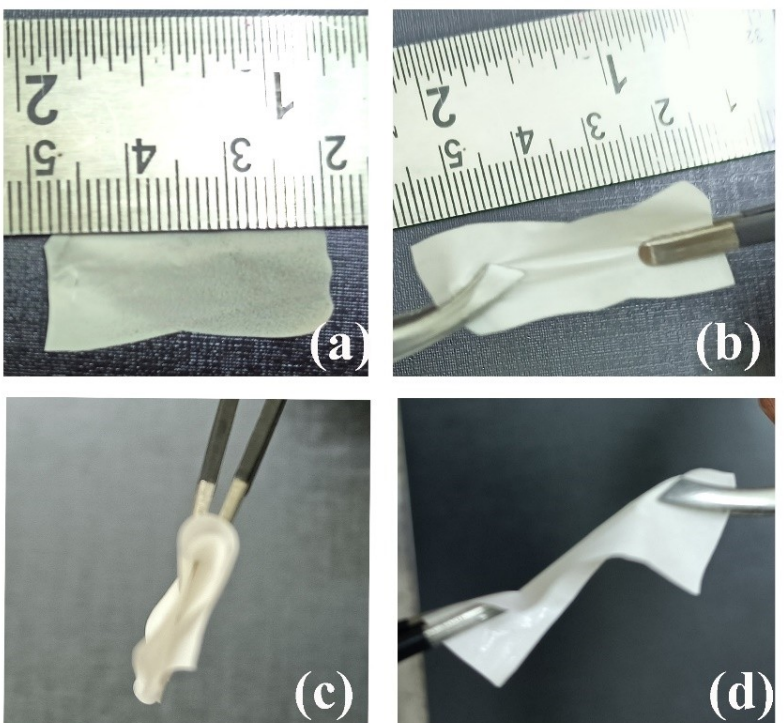


Figure 4. A) Photographs of nanocomposite copolymer membrane with 60 wt% NHIF and under different deforming stresses, namely B) stretching C) folding and D) twisting.

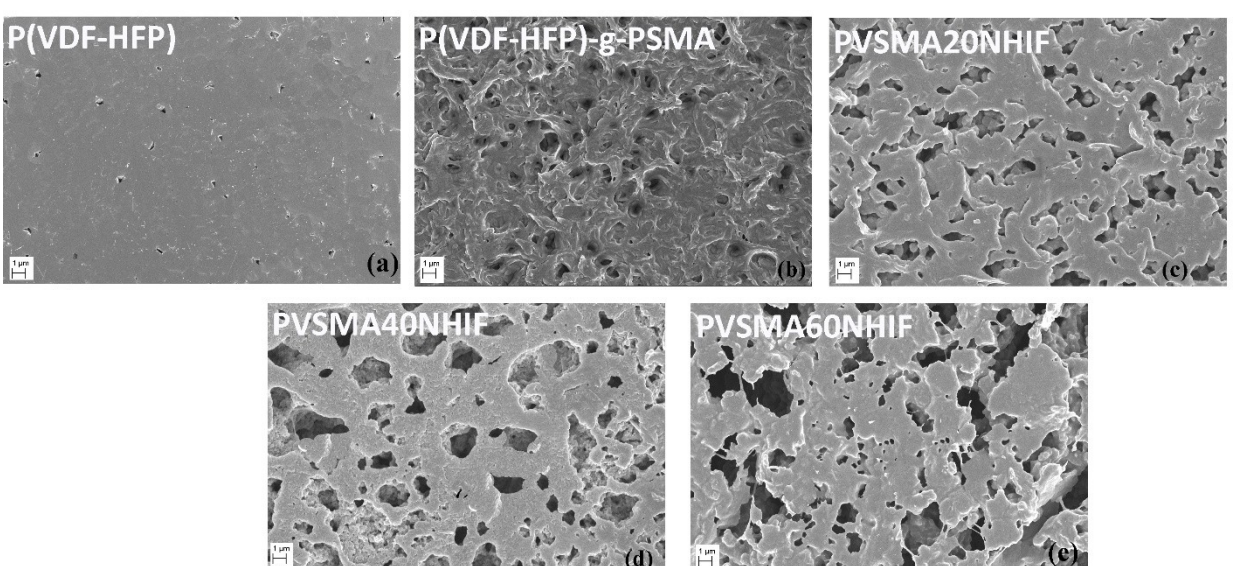


Figure 5. FE-SEM micrographs of different copolymer membranes,

due to the grafting of PSMA side chains in the backbone. Figures 5c to e display the morphology of crosslinked copolymer membranes after the incorporation of different wt% of ZrO₂-NHIF. With increasing NHIF content in the matrix, pores become more extensive and interconnected, indicating the effectiveness of NHIF as a pore-forming agent.

The porosity of the copolymer membranes was further estimated using a simple n-butanol ($M_w \sim 74.12$ g/mol) adsorption method.^[33] In this method, small pieces of membrane were weighed before and after soaking in n-butanol at different time intervals until the weight reached saturation, as shown in Figure S3. The percentage of porosity was determined using eqn. (3)

$$\text{Porosity (\%)} = \frac{(M_w - M_d)/\rho_n}{(M_w - M_d)/\rho_n + M_d/\rho_p} \times 100 \% \quad (3)$$

where M_w and M_d are the weights of the wet and dry film, respectively, ρ_n and ρ_p are the densities of n-butanol and P(VDF-HFP), respectively. In Figure 6a, the variation of porosity (%) estimated from the n-butanol method is shown along with the pore size of the respective membranes obtained from FE-SEM micrographs. It's interesting to observe that raising NHIF content increases both porosity and pore size, which is beneficial concerning the uptake and retention of electrolytes within the membranes.

The uptake and retention of liquid electrolyte 0.5 M LiTFSI salt in [EMIM][TFSI] IL in porous membranes were analyzed by soaking the circularly cut dried membranes of weight W_d in the

electrolyte solution for up to two hours. After different time intervals, the membranes were removed and placed between two sheets of regular paper to absorb any remaining solution on the surface and weighted (W_w). The MGPEs thus formed were then put under a constant pressure of 80 kPa, and the weight of the films was measured (W_0). From those measured weights, the percentage of electrolyte uptake and retention is estimated as^[33–34]

$$\text{ElectrolyteUptake}(W_u)(\%) = \frac{W_w - W_d}{W_d} \times 100 \% \quad (4)$$

$$\text{ElectrolyteRetention}(W_R)(\%) = \frac{W_0 - W_d}{W_w - W_d} \times 100 \% \quad (5)$$

The electrolyte uptake and retention of various membranes are shown in Figures 6b and 6c, respectively. Figure 6d compares the porosity and electrolyte uptake of different membranes. As observed, the pure P(VDF-HFP) membrane shows the lowest electrolyte uptake as it has the lowest porosity with the smallest pore size. Due to the crosslinking and better pore formation, both electrolyte uptake and retention in the SMA-grafted copolymer have improved significantly. With NHIF incorporation, the porosity and electrolyte uptake further enhance, and for PVSMA60NHIF, the electrolyte uptake reaches a maximum value (387%) due to the highest porosity of the membrane (64.5%). Interestingly, apart from superior electrolyte uptake ability, these crosslinked nanocomposite membranes demonstrate impressive electrolyte retentivity (Fig-

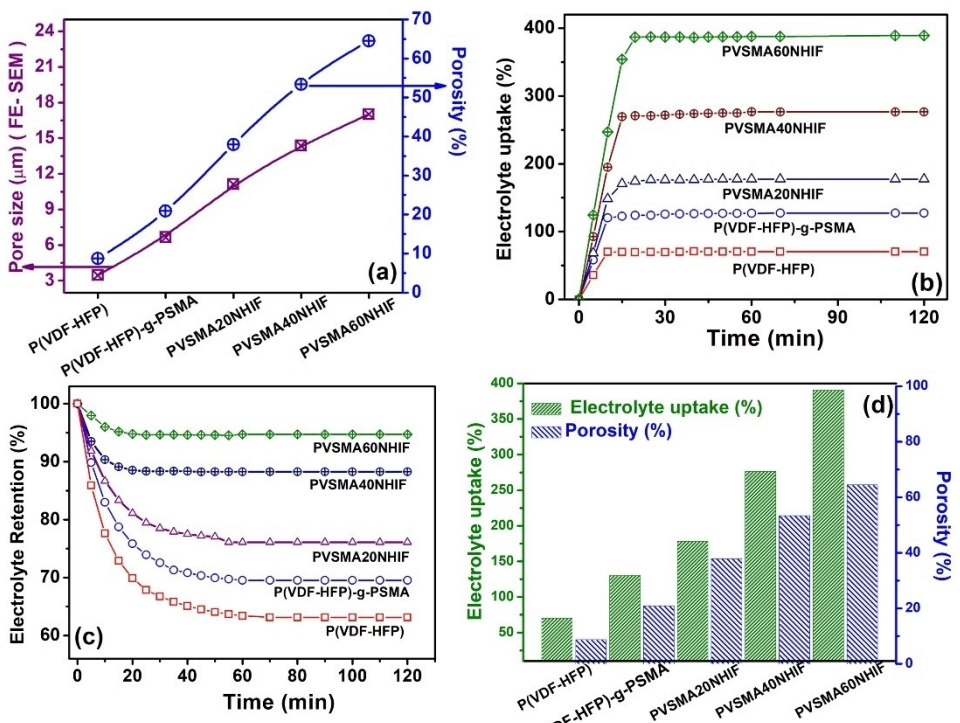


Figure 6. A) Comparison of porosity estimated from FE-SEM micrographs and n-butanol method. B) Electrolyte uptake and C) electrolyte retention as a function of soaking time for different membranes. D) Electrolyte uptake vs porosity for different membranes.

ure 6c). After two hours, the PVSMA60NHIF membrane could retain more than 94% of the soaked electrolyte. Thus, the large pores formed due to NHIF incorporation become interconnected via crosslinking and can hold more electrolytes within the membranes. This is in contrast to the earlier report,^[12b] where the non-interconnected large micropores of the membranes make them vulnerable to leakage with poor electrolyte absorption/retention ability.

Electrical and Electrochemical characterization

Figure 7a shows the inverse temperature variation of DC conductivity of different MGPEs. Each electrolyte shows a typical thermally activated ion conductive nature, i.e., the conductivity

increases with increasing temperature. For MGPE60, the highest conductivity at room temperature (30°C) ($\sim 8.38 \times 10^{-3} \text{ S cm}^{-1}$) has been achieved.

Observed non-Arrhenius type temperature variation of conductivity has been suitably analyzed using the Vogel–Fulcher–Tammann (VFT) equations^[35] expressed as

$$\sigma_{dc} = \sigma_0 \exp(-E_a/k_B(T - T_0)) \quad (6)$$

where E_a is the activation energy for ion conduction and T_0 is the equilibrium glass transition temperature. The solid lines in Figure 7a resemble the best fits of the conductivity data according to Eq. (6) with the fitting parameters as shown in Table 3.

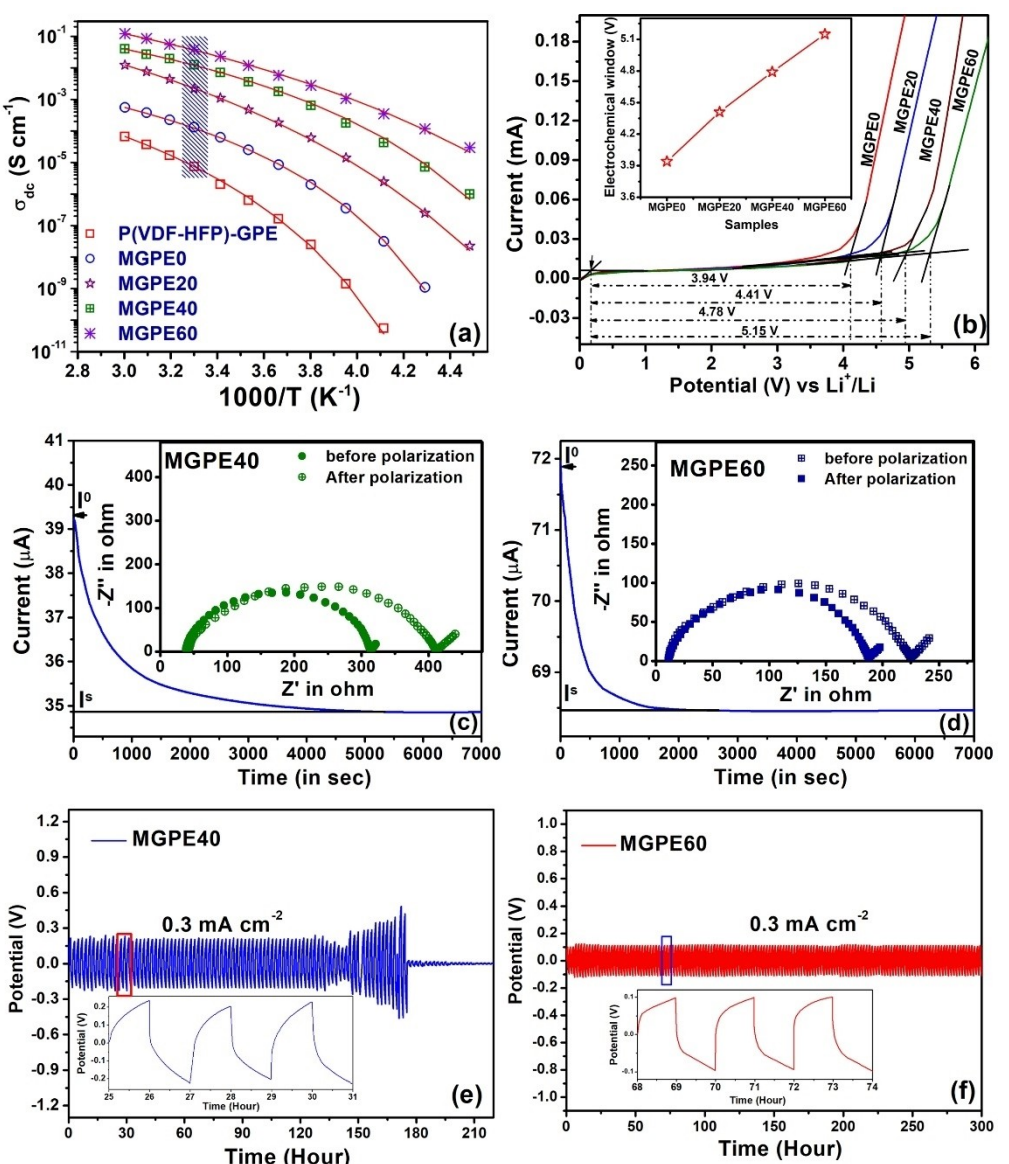


Figure 7. A) Comparison of Arrhenius temperature dependence of ionic conductivities and VFT fitting curves (solid lines) for different MGPEs. B) Electrochemical voltage stability window for different MGPEs. Inset shows the corresponding variation of the voltage window. Chronoamperometry profiles for C) Li/MGPE40/Li and D) Li/MGPE60/Li cells. Insets of the figures show the Nyquist plots of AC impedance before and after polarization and the equivalent circuit used to fit the data. Voltage profiles vs. time of Li symmetric cells comprising E) MGPE40 and F) MGPE60 at a current density of 0.3 mA cm^{-2} .

Table 3. Room temperature ionic conductivity and VFT parameters for different MGPEs. The value of t_{Li^+} for high conducting electrolytes is also listed.					
Samples	$\sigma_{dc}(T = 303K) [\text{mS cm}^{-1}]$ ± 0.03	$\sigma_0 [\text{S cm}^{-1}]$ ± 0.03	$E_a [\text{eV}]$ ± 0.002	$T_0 [\text{K}]$ ± 2.0	t_{Li^+}
P(VDF-HFP)-GPE	0.0083	0.60	0.14	202.0	—
MGPE0	0.079	0.16	0.11	187.2	—
MGPE20	0.38	1.17	0.083	176.9	—
MGPE40	1.91	3.65	0.063	169.3	0.41
MGPE60	5.47	6.58	0.035	161.2	0.64

The excellent agreement of the fitted curves with the experimental data indicates that the ion transport in these electrolytes largely depends upon the ion-hopping process.

The value of both E_a and T_0 gradually reduces with increasing concentrations of NHIF. These indicate that the ZrO_2 -NHIF creates more disordered network structures within the crosslinked copolymer matrix, enabling superior ion transport with lower activation energy. Moreover, higher electrolyte absorption and retention within the crosslinked interconnected porous matrix further improve the overall conductivity in higher NHIF-incorporated GPEs.

An electrolyte must possess a steady and wide electrochemical operating window for the lithium-ion battery application. The linear sweep voltammetry of the SS/MGPE/Li simulated cell explores the electrochemical stability window of the as-prepared MGPEs, as shown in Figure 7b. As observed, with increasing NHIF content, the voltage window gradually improves, and for MGPE60, the electrochemical stability achieves maxima. The electrolyte can withstand more than 5.1 volts vs. Li/Li⁺, which is sufficient for its application with high-voltage electrodes in LIBs.

The higher value of ion conductivity for a dual ion electrolyte does not indicate its higher ability for lithium-ion transport since anions or other existing ions may also contribute to the conductivity. However, the contribution from lithium-ion transport is only beneficial for LIBs, which can be identified from the value of the lithium-ion transference number of the electrolyte (t_{Li^+}). Better lithium ion transport in the electrolyte, designated by a high value of t_{Li^+} reduces the concentration polarization. It restricts the growth of lithium dendrites within the lithium battery, significantly enhancing the cycle performance and cell life.^[36] The t_{Li^+} for different electrolytes was estimated at room temperature by the Bruce method by analyzing the current-time profiles of two different Li/MGPE/Li symmetrical cells together with Nyquist impedance plots before and after the dc polarization, as shown in Figure 7c-d. The interfacial resistances (R_s) of the cells were estimated by analyzing the impedance spectra using the equivalent circuit, as shown in the inset of Figure 7c. The values of t_{Li^+} for the MGPE40, and MGPE60 electrolytes are calculated as 0.41 and 0.64, respectively.

The higher value of t_{Li^+} for MGPEs may be attributed to the inhibiting effect of the movement of TFSI anions within the copolymer network due to the trapping of the anions by the surface functionalized ZrO_2 nanoparticles. In MGPE60, the effect is more significant due to higher content of nanoparticles.

Earlier works also described similar immobilization of anions in gel polymer electrolytes in the presence of nanoparticles.^[12b,37] The significantly lower difference in R_s value for the Li/MGPE60/Li cell as compared to Li/MGPE40/Li obtained from the EIS measurement before and after the polarization indicates the formation of a stable bulk structure and superior interfacial contact of MGPE60 with Li metal as compared to MGPE40. This further designates that MGPE60 may exhibit better electrochemical performances in LMBs. Considering the overall conductivity of the electrolytes at room temperature (303 K) the contribution of conductivity due to Li⁺ ion transport in MGPE40 and MGPE60 has been estimated as $0.95 \times 10^{-3} \text{ S cm}^{-1}$ and $5.38 \times 10^{-3} \text{ S cm}^{-1}$, respectively.

To analyze the sustainability of the MGPEs against continuous plating and stripping of lithium metal, galvanostatic cycling measurements are carried out at room temperature on symmetric Li/MGPE/Li cells at 0.3 mA cm^{-2} constant current density with an areal specific capacity of 0.3 mAh cm^{-2} . Figures 7e and 7f depict the time-dependent voltage profiles of the cells. With both the MGPEs, the first Li plating process starts with a smooth and steady increase in potential, indicating the formation of smooth interphase on the Li-metal electrode after the cell preparation. As shown in Figure 7e, the initial overpotential of the MGPE40 cell is about 190 mV, and the cell failed after 180 hours due to sudden rise in overpotential. Some voltage oscillations were also observed during the plating/stripping process, indicating instability at the interface. On the other hand, the MGPE60 cell (Figure 7f) delivers a low and very stable voltage hysteresis within 100 mV with minimum oscillations up to 300 h cycling, demonstrating the non-occurrence of any dendritic deposition during the plating/stripping process. A slight decrease in overpotential up to the initial few cycles for both cells is attributed to the activation of the pristine oxide layer on the Li anode surface.^[38] The observed results confirm that the content of NHIF in MGPE has a significant impact on the overall lithium ion transport and interfacial phenomena. Higher NHIF content not only improves the t_{Li^+} value but also promotes the formation of a stable electrolyte/Li interface.

Electrochemical performance of the lithium-polymer battery

The all-solid-state Li metal batteries consisting of LiFePO₄ cathode (LFP) are assembled to evaluate the electrochemical performance of the MGPEs. The rate performance of LFP/Li cells

comprising MGPE60 and MGPE40 electrolytes is demonstrated in Figure 8a. In Figure 8b and Figure S4a, respectively, the charge/discharge performance of the cells at various current rates in the operating voltage window of 2.4–4.0 V is displayed. As can be observed, the discharge capacity of the MGPE60 cell at 0.1 C, 0.2 C, 0.5 C, 1 C, and 2 C is 161.2 mAh g^{-1} , 158.5 mAh g^{-1} , 153.2 mAh g^{-1} , 146.1 mAh g^{-1} and 135.6 mAh g^{-1} , respectively, which is significantly higher than that of the MGPE40 cell at these rates.

Moreover, as observed from Figure 8c, the MGPE60 electrolyte allows the Li/LFP cell to exhibit a significantly lower overpotential (0.17 V) as compared to the MGPE40-based cell (0.26 V). The difference in discharge capacity for the cells becomes more prominent at a current rate of 1.0 C or higher. Moreover, when the rate returns to 0.1 C , the MGPE60 cell could successfully regain its initial discharge capacity. The MGPE40 cell, on the other hand, is unable to attain such

excellent reversibility and displays a lower discharge capacity than its initial value.

The long-term cycle performance at 0.5 C rate and the corresponding charge/discharge profiles for MGPE60 and MGPE40 cells are presented in Figures 8d, 8e, and Figure S4(b), respectively. Even after 100 cycles, the Li/MGPE60/LFP cell exhibits a discharge capacity of 149.3 mAh g^{-1} ($>96\%$ of the initial value), with $>99\%$ Coulombic efficiency. Contrarily, after 100 cycles at 0.5 C , the LFP/MGPE40/Li cell could retain only 88% of the initial discharge capacity with a degraded Coulombic efficiency of $\sim 95.0\%$. The observed exceptional long-term cycle stability of the LFP/MGPE60/Li cell indicates the formation of relatively better electrode/electrolyte interfacial stability within it. This may be attributed to the better electrode/electrolyte interfacial compatibility and high lithium ionic conductivity of the electrolyte's, which allow lithium ions to be moved evenly and fast inside the cell.

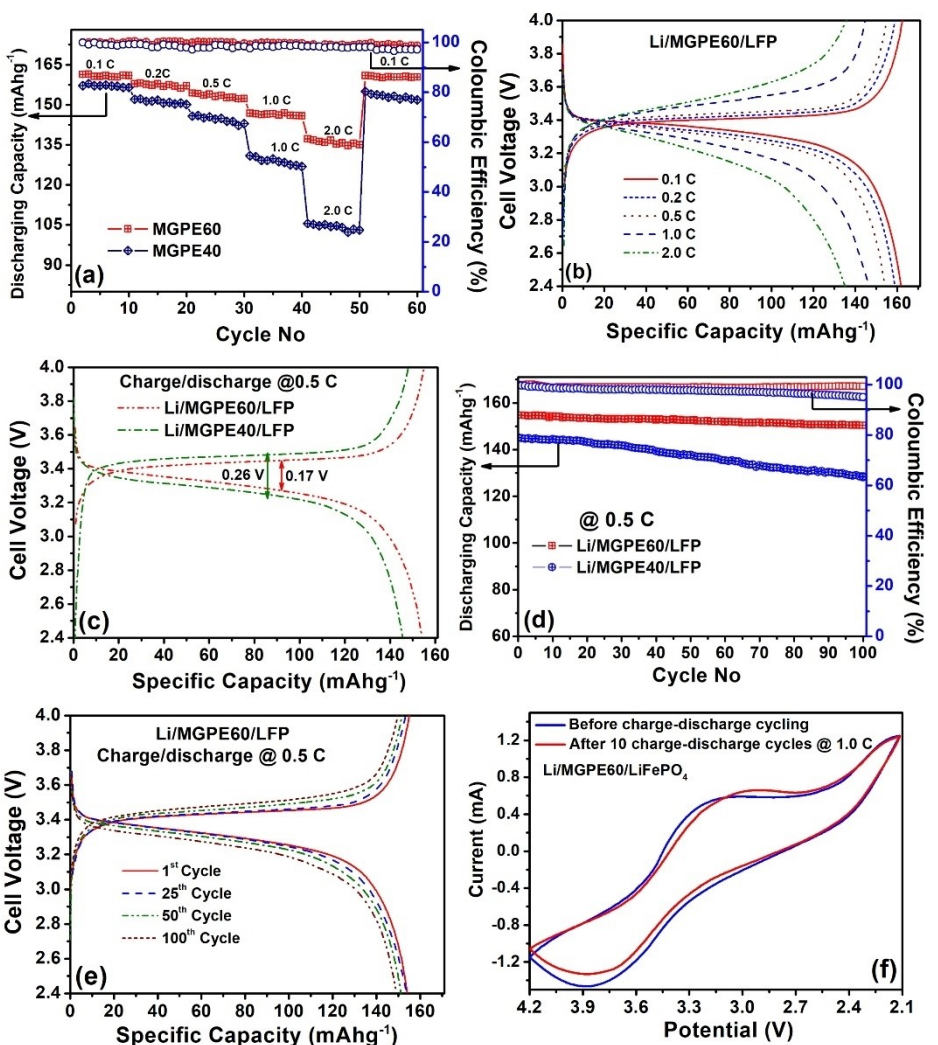


Figure 8. Electrochemical performances of all-solid-state $\text{LiFePO}_4/\text{Li}$ cells with MGPE60 and MGPE40 electrolytes A) Rate performance of $\text{LiFePO}_4/\text{Li}$ cells. B) Charge-discharge voltage profiles of $\text{LiFePO}_4/\text{MGPE60}/\text{Li}$ cell at various rates. Comparison of C) Charge-discharge voltage profiles and D) cycling performance of $\text{LiFePO}_4/\text{MGPE40}/\text{Li}$ and $\text{LiFePO}_4/\text{MGPE60}/\text{Li}$ cells at 0.5 C . E) long-term charge-discharge voltage profiles of $\text{LiFePO}_4/\text{MGPE60}/\text{Li}$ cell at 0.5 C . F) Cyclic voltammetry (CV) before and after the charge/discharge cycles of $\text{Li}/\text{MGPE60}/\text{LFP}$ cell within the potential range, $2.1\text{--}4.2 \text{ V}$ at a scan rate of 0.1 mV s^{-1} .

To further demonstrate the applicability of the MGPE60 in the LMBs, the Li/MGPE60/LFP cell was evaluated via cyclic voltammetry in a voltage range of 2.1–4.2 V at a scan rate of 0.1 mVs⁻¹. Figure 8f shows the CV comparison of the LFP/MGPE60/Li cell before and after cycling for 10 cycles at a considerably high charge-discharge rate (1.0 C). As can be observed, the CV curves do not show significant change before and after the cycle and only have one pair of redox peaks. This indicates that the Li/MGPE60/LFP cell does not undergo any side reactions during charging and discharging, even at a high current rate.

Motivated by the above brilliant electrochemical performances of the MGPE60 electrolyte in Li/LFP cell, the compatibility and rate performance of the electrolyte in a lithium battery comprising high voltage NMC811 cathode material have also been analyzed. Figures 9a and 9b demonstrate the rate capability and charge/discharge cycles of Li/MGPE60/NCM811 battery at different current rates within the voltage range of 2.5–4.5 V. As observed, the cell delivers a high specific capacity of 197.5 mAhg⁻¹, 189.2 mAhg⁻¹, 174.4 mAhg⁻¹, 156.5 mAhg⁻¹,

and 125.6 mAhg⁻¹ at 0.1 C, 0.2 C, 0.5 C, 1 C, and 2 C, respectively, with 99 % Coulombic efficiency. The voltage polarization gradually increases with the discharging C-rates, and a distinct potential plateau can be seen up to 1 C rate. In addition, when the rate returns to 0.1 C, the discharge capacity and Coulombic efficiency remain at 191.4 mAhg⁻¹ and 99.1 %, respectively.

The cycling performance of the cell at 0.5 C is shown in Figure 9c. After 100 cycles, the cell is able to retain > 84.0 % of its initial value (Figure 9d). However, the Coulomb efficiency of the cell during the cycle has always been maintained at ~99.0 %. Such exceptional cycle stability of the cell suggests that a stable interface has formed between the MGPE60 electrolyte and the high-voltage cathode, which is further supported by the potentiostatic EIS study of the cell. Figure 9e shows the Nyquist EIS plots measured after different discharge cycles of the Li/MGPE60/NMC811 cell. From the analysis of the EIS spectra using the equivalent circuit as shown in the inset, different parameters, viz, the electrode/electrolyte interfacial impedance (R_{ct}) and bulk impedance (R_b) of the cell, are evaluated as shown in Figure 9f. For the fresh cell, the values of

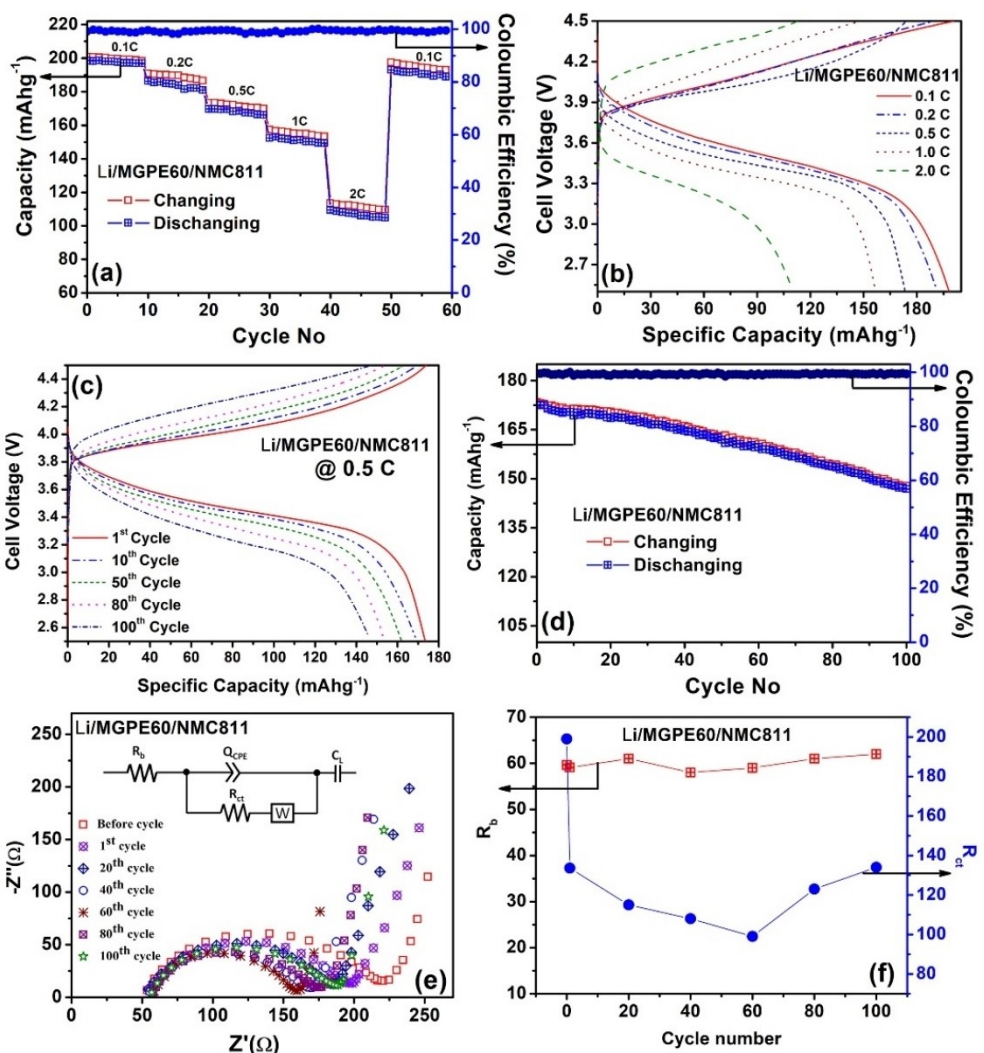


Figure 9. Electrochemical performances of all-solid-state NMC811/Li cells with MGPE60 electrolyte A) Rate performance; B) Charge-discharge voltage profiles at various

R_b and R_{ct} is found to be $59\ \Omega$ and $199\ \Omega$, respectively. During the cycle operation, the value of R_b does not change appreciably, indicating better stability of the MGPE60 electrolyte. On the other hand, the R_{ct} value drops to $\sim 134\ \Omega$ after the 1st discharge cycle due to the formation of a solid electrolyte interface (SEI).^[10a,39] The Li/MGPE60/NMC811 cell exhibits the development of a stable electrode/electrolyte interface inside of it, with a continuous decline in R_{ct} value up to 60 cycles, reaching a minimum value of $99.5\ \Omega$, above which the trend reverses. Thus, apart from the high lithium ion transfer ability of the MGPE60 electrolyte, its excellent interfacial compatibility with both low and high-voltage electrolytes extends the application potentiality of the stearyl methacrylate grafted P(VDF-HFP) nanocomposite membrane-based GPE for high-performance lithium batteries.

Conclusions

In conclusion, a novel microporous organic-inorganic hybrid polymer membrane with a crosslinked branching structure was developed by grafting stearyl methacrylate onto the P(VDF-HFP) copolymer backbone, followed by blending with uniformly dispersed ionic liquid functionalized ZrO_2 nanoparticles (ZrO_2 -NHIF). The structural, morphological, thermal, and crystallinity behaviors of the membranes were systematically characterized. The study revealed that the secondary block, SMA, with its large non-polar units, disrupts the typical packing of P(VDF-HFP) chains, which on the one hand reduces the crystallinity of the system and on the other hand enhances the porosity. ZrO_2 -NHIF blending boosted both the process to produce a highly porous and amorphous network structure. Different quasi-solid-state microporous gel polymer electrolytes were prepared by soaking the membranes in LiTFSI salt-dissolved imidazolium ionic liquid-based electrolyte. The optimized thermally stable, free-standing nanocomposite copolymer membrane (PVSMA60NHIF) with the highest porosity of 64.5% demonstrated the maximum electrolyte uptake ability (387 wt.%) with $\sim 94\%$ retentivity, which allowed the corresponding gel polymer electrolyte (MGPE60) to exhibit the highest ionic conductivity of $\sim 5.34 \times 10^{-3}\ \text{Scm}^{-1}$ at room temperature (303 K) along with a high lithium-transference number of nearly 0.64 and a wide electrochemical stability window of $> 5.1\ \text{V}$ vs Li/Li⁺. The lithium metal battery assembled with a lithium anode, MGPEs, and LiFePO₄ cathode exhibited excellent rate capability, cycling stability, and a high coulombic efficiency of $\sim 99.2\%$ for each cycle. The cell also demonstrated improved cycling performance with $> 96\%$ capacity retentivity at 0.5 C after 100 cycles. Moreover, the electrolyte showed excellent interfacial compatibility with high voltage cathode material (NMC811), and the Li|MGPE60|NMC811 cell delivered an excellent reversible specific capacity of $\sim 190\ \text{mAhg}^{-1}$ at 0.1 C and displayed a reasonable cycling performance with more than 85% capacity retention ability at 0.5 C after 100 cycles. The study established that long-chain non-polar branching with a macromolecular copolymer host enables the pore-forming agents to act effectively to create better porosity in the membrane for superior electrolyte

uptake and retention ability. This allowed the associated MGPEs to display superior Li⁺ ion transfer capabilities with the creation of a stable Li/electrolyte interface, which consequently improved the overall electrochemical performance of the lithium metal batteries.

Acknowledgements

The authors thankfully acknowledge the grant received from SERB, Government of India (File No: CRG/2019/005894).

Conflict of Interests

The authors declare no conflict of interest.

Data Availability Statement

The data that support the findings of this study are available on request from the corresponding author. The data are not publicly available due to privacy or ethical restrictions.

Keywords: Ionic liquid functionalized nanoparticles • grafted copolymer nanocomposite membranes • microporous gel polymer electrolyte • lithium battery • interfacial compatibility

- [1] a) W. Lu, Z. Yuan, Y. Zhao, H. Zhang, H. Zhang, X. Li, *Chem. Soc. Rev.* **2017**, *46*, 2199–2236; b) Y.-S. Oh, G. Y. Jung, J.-H. Kim, J.-H. Kim, S. H. Kim, S. K. Kwak, S.-Y. Lee, *Adv. Funct. Mater.* **2016**, *26*, 7074–7083.
- [2] C. M. Costa, Y.-H. Lee, J.-H. Kim, S.-Y. Lee, S. Lanceros-Méndez, *Energy Storage Mater.* **2019**, *22*, 346–375.
- [3] a) Y. Yang, W. Wang, G. Meng, J. Zhang, *J. Mater. Chem. A* **2022**, *10*, 14137–14170; b) A. Celik-Kucuk, T. Abe, *Batteries & Supercaps* **2023**, *6*, e202300183.
- [4] a) N. Nitta, F. Wu, J. T. Lee, G. Yushin, *Mater. Today* **2015**, *18*, 252–264; b) M. M. Huie, R. A. DiLeo, A. C. Marschilok, K. J. Takeuchi, E. S. Takeuchi, *ACS Appl. Mater. Interfaces* **2015**, *7*, 11724–11731.
- [5] J. M. Tarascon, A. S. Gozdz, C. Schmutz, F. Shokoohi, P. C. Warren, *Solid State Ionics* **1996**, *86–88*, 49–54.
- [6] a) M. Li, Y. Liao, Q. Liu, J. Xu, P. Sun, H. Shi, W. Li, *Electrochim. Acta* **2018**, *284*, 188–201; b) D. Deb, P. Bose, S. Bhattacharya, *Ionics* **2021**, *27*, 123–136.
- [7] C. F. J. Francis, I. L. Kyrtzis, A. S. Best, *Adv. Mater.* **2020**, *32*, 1904205.
- [8] J. Kalhoff, G. T. Kim, S. Passerini, G. Appetecchi, *J. Power Energy Eng.* **2016**, *04*, 9–18.
- [9] a) D. Deb, P. Bose, S. Bhattacharya, *Int. J. Energy Res.* **2020**, *44*, 10506–10522; b) A. Hofmann, M. Schulz, T. Hanemann, *Electrochim. Acta* **2013**, *89*, 823–831.
- [10] a) P. Bose, D. Deb, S. Bhattacharya, *J. Power Sources* **2018**, *406*, 176–184; b) D. Deb, S. Bhattacharya, *J. Mol. Liq.* **2023**, *379*, 121645.
- [11] a) C. S. Stefan, D. Lemordant, B. Claude-Montigny, D. Violeau, *J. Power Sources* **2009**, *189*, 1174–1178; b) M. Kirchhöfer, J. Von Zamory, E. Paillard, S. Passerini, in *International Journal of Molecular Sciences*, Vol. *15*, **2014**, pp. 14868–14890.
- [12] a) Z. Ren, K. Sun, Y. Liu, X. Zhou, N. Zhang, X. Zhu, *Solid State Ionics* **2009**, *180*, 693–697; b) P. Bose, D. Deb, S. Bhattacharya, *Electrochim. Acta* **2019**, *319*, 753–765.
- [13] a) M. R. Asghar, Y. Zhang, A. Wu, X. Yan, S. Shen, C. Ke, J. Zhang, *J. Power Sources* **2018**, *379*, 197–205; b) Z. Tabani, H. Maghsoudi, A. Fathollahi-Zonouz, *J. Solid State Electrochem.* **2021**, *25*, 651–657.
- [14] L. Gu, M. Zhang, J. He, P. Ni, *Electrochim. Acta* **2018**, *292*, 769–778.
- [15] S. Liang, Y. Shi, T. Ma, W. Yan, S. Qin, Y. Wang, Y. Zhu, H. Wang, Y. Wu, *ChemElectroChem* **2019**, *6*, 5413–5419.

- [16] a) J. Zhang, C. Zhu, J. Xu, J. Wu, X. Yin, S. Chen, Z. Zhu, L. Wang, Z.-C. Li, *J. Membr. Sci.* **2020**, *597*, 117622; b) Y.-Y. Lee, Y.-L. Liu, *Electrochim. Acta* **2017**, *258*, 1329–1335.
- [17] a) S. Song, X. Tan, Y. Zhai, G. Yang, J. Yao, S. Li, N. Hu, X. Qi, R. Li, W. Ma, Z. Wen, L. Lu, *ChemElectroChem* **2020**, *7*, 3656–3662; b) P. Zhang, L. C. Yang, L. L. Li, M. L. Ding, Y. P. Wu, R. Holze, *J. Membr. Sci.* **2011**, *379*, 80–85; c) H. T. T. Le, D. T. Ngo, R. S. Kalubarme, G. Cao, C.-N. Park, C.-J. Park, *ACS Appl. Mater. Interfaces* **2016**, *8*, 20710–20719.
- [18] a) J. T. Park, J. H. Koh, D. K. Roh, Y. G. Shul, J. H. Kim, *Int. J. Hydrogen Energy* **2011**, *36*, 1820–1827; b) Z. Cui, E. Drioli, Y. M. Lee, *Prog. Polym. Sci.* **2014**, *39*, 164–198; c) L. Xie, X. Huang, K. Yang, S. Li, P. Jiang, *J. Mater. Chem. A* **2014**, *2*, 5244–5251.
- [19] a) B. Dutta, D. Deb, S. Bhattacharya, *Int. J. Hydrogen Energy* **2018**, *43*, 4081–4089; b) D. Deb, S. Bhattacharya, *J. Phys. Chem. C* **2017**, *121*, 6962–6976; c) B. Dutta, D. Deb, S. Bhattacharya, *J. Mater. Sci.* **2019**, *54*, 2990–3008.
- [20] J. Zhang, C. Ma, Q. Xia, J. Liu, Z. Ding, M. Xu, L. Chen, W. Wei, *J. Membr. Sci.* **2016**, *497*, 259–269.
- [21] a) P. E. Trapa, Y.-Y. Won, S. C. Mui, E. A. Olivetti, B. Huang, D. R. Sadoway, A. M. Mayes, S. Dallek, *J. Electrochem. Soc.* **2005**, *152*, A1; b) C. Ma, J. Zhang, M. Xu, Q. Xia, J. Liu, S. Zhao, L. Chen, A. Pan, D. G. Ivey, W. Wei, *J. Power Sources* **2016**, *317*, 103–111; c) M. Tao, F. Liu, L. Xue, *J. Mater. Chem.* **2012**, *22*, 9131–9137; d) L. Zhou, H. Zhao, K. Liang, J. Chen, J. Li, X. Huang, Y. Qi, Y. Ren, *J. Colloid Interface Sci.* **2022**, *613*, 606–615.
- [22] P. Bose, S. Bhattacharya, *Int. J. Hydrogen Energy* **2018**, *43*, 4090–4100.
- [23] D. Deb, S. Bhattacharya, *Electrochim. Acta* **2017**, *245*, 438–447.
- [24] J. W. Evans, C. A. Vincent, P. G. Bruce, *Polymer* **1987**, *28*, 2324–2328.
- [25] a) M.-S. Zheng, J.-W. Zha, Y. Yang, P. Han, C.-H. Hu, Y.-Q. Wen, Z.-M. Dang, *Appl. Phys. Lett.* **2017**, *110*, 252902; b) J. Zhou, L. Wang, C. Wang, T. Chen, H. Yu, Q. Yang, *Polymer* **2005**, *46*, 11157–11164; c) S. Golcuk, A. E. Muftuoglu, S. U. Celik, A. Bozkurt, *J. Polym. Res.* **2013**, *20*, 144.
- [26] Q. Hu, S. Osswald, R. Daniel, Y. Zhu, S. Wesel, L. Ortiz, D. R. Sadoway, *J. Power Sources* **2011**, *196*, 5604–5610.
- [27] N. Angulakshmi, S. Thomas, K. S. Nahm, A. M. Stephan, R. N. Elizabeth, *Ionics* **2011**, *17*, 407–414.
- [28] P. Martins, A. C. Lopes, S. Lanceros-Mendez, *Prog. Polym. Sci.* **2014**, *39*, 683–706.
- [29] V. Jovanovski, B. Orel, R. Ješe, A. Šurca Vuk, G. Mali, S. B. Hočevar, J. Grdadolnik, E. Stathatos, P. Lianos, *J. Phys. Chem. B* **2005**, *109*, 14387–14395.
- [30] M. C. Kuo, J. C. Huang, M. Chen, *Mater. Chem. Phys.* **2006**, *99*, 258–268.
- [31] C. Marega, A. Marigo, *Eur. Polym. J.* **2003**, *39*, 1713–1720.
- [32] M. Ciosek, L. Sannier, M. Siekierski, D. Golodnitsky, E. Peled, B. Scrosati, S. Glowinkowski, W. Wieczorek, *Electrochim. Acta* **2007**, *53*, 1409–1416.
- [33] F. Deng, X. Wang, D. He, J. Hu, X. Xie, Z. Xue, *J. Membr. Sci.* **2015**, *491*.
- [34] T. Yang, C. Shu, R. Zheng, A. Hu, Z. Hou, M. Li, Z. Ran, P. Hei, J. Long, *J. Membr. Sci.* **2020**, *604*, 118051.
- [35] C. A. Angell, *J. Non-Cryst. Solids* **1991**, *131*–133, 13–31.
- [36] X. Zeng, L. Dong, J. Fu, L. Chen, J. Zhou, P. Zong, G. Liu, L. Shi, *Chem. Eng. J.* **2022**, *428*, 131100.
- [37] S.-H. Wang, Y.-Y. Lin, C.-Y. Teng, Y.-M. Chen, P.-L. Kuo, Y.-L. Lee, C.-T. Hsieh, H. Teng, *ACS Appl. Mater. Interfaces* **2016**, *8*, 14776–14787.
- [38] J. Wu, X. Wang, Q. Liu, S. Wang, D. Zhou, F. Kang, D. Shanmukaraj, M. Armand, T. Rojo, B. Li, G. Wang, *Nat. Commun.* **2021**, *12*, 5746.
- [39] R. Verrelli, B. Scrosati, Y.-K. Sun, J. Hassoun, *ACS Appl. Mater. Interfaces* **2014**, *6*, 5206–5211.

Manuscript received: November 1, 2023

Revised manuscript received: January 29, 2024

Accepted manuscript online: February 7, 2024

Version of record online: February 19, 2024